

# Structural correlations of nitrogenase active sites using nuclear resonance vibrational spectroscopy and QM/MM calculations†

Casey Van Stappen,                                <img alt="Google Scholar icon" data-bbox="9417 271 9437 29

## Introduction

Nitrogenase ( $\text{N}_2$ ase) is a microbial enzyme responsible for converting inert atmospheric dinitrogen ( $\text{N}_2$ ) to bioavailable ammonia ( $\text{NH}_3$ ) under ambient conditions.<sup>1,2</sup> The industrial analogue of this reaction is the Haber-Bosch (HB) process, which is energy-intensive and environmentally taxing due to the high pressures (>100 bar) and temperatures ( $\sim 500^\circ\text{C}$ ) used during catalysis, and the significant quantities of  $\text{CO}_2$  produced as a by-product of industrial  $\text{H}_2$  production.<sup>3,4</sup> The ambient,  $\text{H}_2$ -free nature of  $\text{N}_2$ ase-catalyzed nitrogen fixation has made these enzymes particularly alluring in the search for alternative routes to  $\text{NH}_3$  production, both for fertilizer production and as an  $\text{H}_2$  carrier. Furthermore,  $\text{N}_2$ ases can catalytically reduce several triple bond-containing substrates, including  $\text{HCN}$ ,  $\text{C}_2\text{H}_2$ ,  $\text{N}_3^-$ , and even inert  $\text{CO}$ .<sup>5-7</sup>

Three types of nitrogenases have been reported, each named for the homocitrate-binding metal contained in the catalytic cofactor, *i.e.*, Mo, V, and Fe  $\text{N}_2$ ase. Each of these three nitrogenases is a two-component system, comprised of a reducing Fe-protein, and the catalytic cofactor-containing MFe protein ( $\text{M} = \text{Mo, V, Fe}$ ), again denoted by the contained homocitrate-binding metal (Fig. 1).<sup>8,9,12,13</sup> Similarly, the catalytic clusters of MoFe, VFe, and FeFe are referred to as FeMoco ( $[\text{Mo-7Fe-9S-C-homocitrate}]$ ), FeVco ( $[\text{V-7Fe-8S-C-(CO}_3\text{-homocitrate}]$ ), and FeFeco (putative composition:  $[\text{8Fe-9S-C-homocitrate}]$ ), respectively. Extensive kinetic, spectroscopic

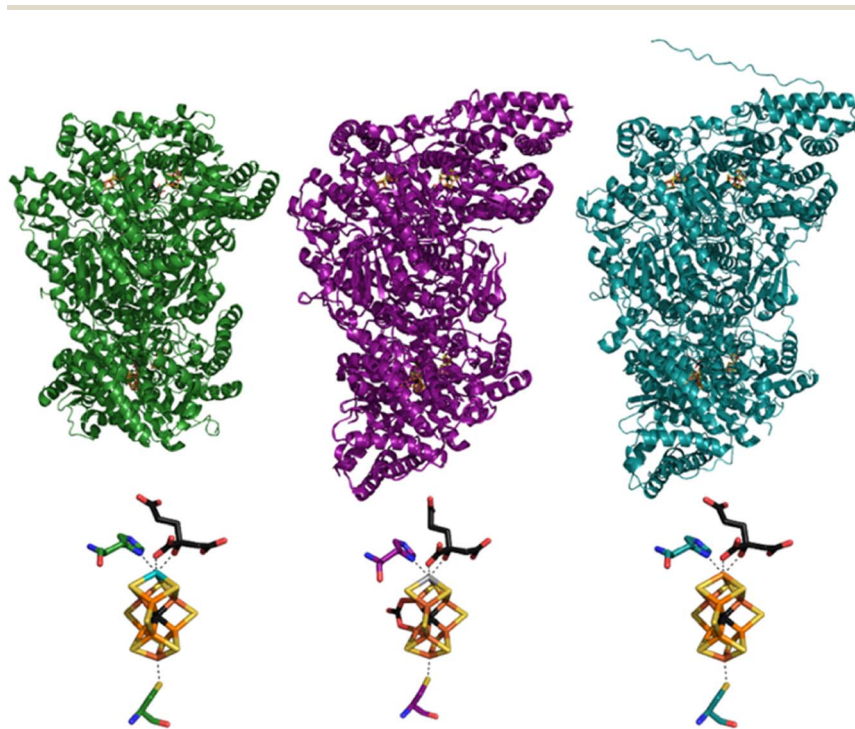


**Fig. 1** Structural models of the MoFe (green, PDB ID: 3U7Q8), VFe (purple, PDB ID: 5N6Y9), and FeFe (teal) proteins (top) and of their catalytic FeMoco clusters, coordinated to homocitrate and the histidine and cysteine residues (bottom). The displayed FeFe model was generated using AlphaFold and the protein sequence of FeFe.<sup>10,11</sup>



and crystallographic studies have been performed on Mo N<sub>2</sub>ase to explore the structure and reactivity of both the resting state and catalytic intermediates;<sup>7,14–20</sup> however, significantly fewer studies have focused on VN<sub>2</sub>ase,<sup>21–25</sup> and even less on Fe N<sub>2</sub>ase.<sup>13,14,26–28</sup> Interestingly, all three N<sub>2</sub>ases exhibit significant differences in their catalytic reactivity towards N<sub>2</sub> and alternative substrates,<sup>7,29</sup> and the relationships between cofactor structure and activity are not yet well understood.

Valence-to-Core X-ray Emission Spectroscopy (VtC XES) measurements have established that the cofactors of all three N<sub>2</sub>ases contain a central carbide atom,<sup>25,28,30</sup> and high-resolution crystal structures of the MoFe and VFe proteins have further shown that the interstitial carbide atom exists in a unique hexacoordinated fashion between six Fe in a prismatic geometry.<sup>8,9</sup> However, the role of the carbide atom during catalysis is still unclear. Recently, Hoffman and co-workers have extensively employed ENDOR spectroscopy across multiple redox states and intermediates of Mo N<sub>2</sub>ase to establish that the carbide atom serves to maintain the structural rigidity of the cofactor (acting as a “heart of steel”).<sup>31</sup> Seven different protein samples were investigated, including both resting and reactive intermediate states, and the <sup>13</sup>C isotopic hyperfine coupling constants were found to range from –1.3 to +2.7 MHz, indicating negligible changes to the carbide structure for Mo N<sub>2</sub>ase during turnover. Meanwhile, FeVco was long believed to be a direct analog of FeMoco, with V replacing Mo at the apical position of the cluster, however, crystal structures of the VFe protein have unexpectedly and consistently revealed that one of three belt sulfurs of FeVco is replaced by a carbonate ligand.<sup>9,22–24</sup> We note however, that spectroscopic support for the presence of the carbonate bridge remains elusive.<sup>28</sup> Meanwhile, the crystal structure of the FeFe protein has yet to be reported in the literature.

Despite significant progress in the active site structure characterization of N<sub>2</sub>ases, particularly through protein crystallography, extensive X-ray spectroscopy, and pulsed EPR methods, a comparative study of all three N<sub>2</sub>ases using an Fe-specific spectroscopic tool to examine the structural differences of the three unique catalytic cofactors has yet to be reported. All three unique catalytic cofactors of the N<sub>2</sub>ases share Fe as the primary metal component; therefore, Fe-specific techniques, such as <sup>57</sup>Fe nuclear resonance vibrational spectroscopy (NRVS),<sup>32–35</sup> can serve as common probes of the active sites of all three N<sub>2</sub>ases, allowing their molecular and electronic structures to be compared. Herein, we report the NRVS characterization of MoFe together with the “alternative nitrogenases” (V-, Fe-dependent N<sub>2</sub>ases). For each of the three nitrogenases, we present both the apo (FeMco-deficient, M = Mo, V, Fe) and holo proteins. In this way, we determine the primary spectral regions where the FeMco-clusters and P-clusters contribute to the partial vibrational density of states (PVDOS), and further correlate these results with electronic structure investigations at the QM/MM level. The sensitivity of the calculated PVDOS to the computational model parameters are discussed, and the implications of these findings for structural modelling based on NRVS data are highlighted.

## Materials and methods

### Protein sample preparation

The strep-tagged holo-MoFe, apo-MoFe, holo-VFe, apo-VFe, holo-FeFe and apo-FeFe proteins were produced in *Azotobacter vinelandii* strains DJ2102, DJ2115,



DJ2253, DJ2256, DJ2241 and DJ2245 (generously provided by Prof. Dennis Dean), respectively, in  $^{57}\text{Fe}$ -enriched media following published procedures.<sup>36,37</sup> Proteins were isolated from cell pellets as follows: cells were resuspended and lysed in Bug Buster Master Mix solution (Merck Millipore, 4 : 1 v/w) following manufacturer's instructions, then the lysate was centrifuged at 45 000 rpm using a Ti 70 rotor. The soluble fraction was loaded on a 10 mL gravity-flow Strep-tactin column previously equilibrated in buffer [Tris 20 mM pH 7.4, NaCl 200 mM]. The column was then washed with the same buffer until the flow-through did not contain any protein, and the protein was eluted with 30 mL of that buffer supplemented with 3 mM desthiobiotin. The elution fraction was concentrated using a 100 kDa MWCO centrifugal filter unit until a concentration of 80 mg  $\text{mL}^{-1}$ . 5 mM Na dithionite was added to each sample before loading in NRVS sample cells. For measurements at SPring-8 BL19LXU, the sample cells consisted of a 16.6  $\times$  3.6  $\times$  2.4 mm ( $l \times w \times h$ ) block Delrin® with a 10  $\times$  3  $\times$  1.2 mm ( $l \times w \times h$ ) well machined into the face. For measurements at ESRF ID18, sample cells consisted of a Cu block with a machined 12  $\times$  2.5  $\times$  1.5 mm trough, which was coated with a thin polystyrene film to prevent direct contact of the sample with metallic Cu. The open faces of the well/trough of either sample cell were sealed with 1-mil (25  $\mu\text{m}$ ) polyimide tape prior to sample loading, which was performed using a Hamilton® syringe and stainless-steel needle.

### NRVS data collection & analysis

$^{57}\text{Fe}$  NRVS spectra of holo-VFe, apo-VFe, holo-FeFe and apo-FeFe proteins were measured at SPring-8 BL19LXU, while measurements of holo-MoFe and apo-MoFe proteins were performed at ESRF ID18. Detailed descriptions of the experimental setups used at either beamline are provided in the ESI.† NRVS data analysis includes aligning, summing, and normalizing scans, deconvoluting the monochromator line shape function, subtracting the intensity from the elastic nuclear resonance, estimation of sample temperature by detailed balance fitting, removal of multi-phonon contributions, and conversion to the PVDOS. For spectra obtained at SPring-8 BL19LXU, these steps were performed using the padd and phox subroutines of the program PHOENIX v. 2.1.4.<sup>38,39</sup> For spectra obtained at ESRF ID18, these steps were performed using the software package DOS<sup>40</sup> updated with the graphical user interface nisGUI v. 1.2. Additionally, energy calibration was performed in MATLAB based on measurements of  $[\text{Et}_4\text{N}]^{57}\text{FeCl}_4$  based on the reported  $\text{T}_2$  bending mode at 138  $\text{cm}^{-1}$  and asymmetric  $\text{T}_2$  stretching modes at 376 and 389  $\text{cm}^{-1}$ .<sup>41</sup>

The derived FeMoco PVDOS was calculated using the normalized probability densities of the nuclear inelastic absorption spectra acquired for apo- and holo-MoFe. Specifically, the spectrum of apo-MoFe was scaled by 8/15ths (corresponding to 8 Fe of the P-cluster contributing to the 15 Fe contained in holo-MoFe) and numerically subtracted from the spectrum of holo-MoFe. The resulting difference spectrum was then processed using the phox subroutine of the program PHOENIX v. 2.1.4 to produce the PVDOS.<sup>38,39</sup>

### QM/MM calculations of $^{57}\text{Fe}$ PVDOS

Quantum mechanics/molecular mechanics (QM/MM) models of MoFe and VFe protein from previous studies were used.<sup>42,43</sup> FeFeco QM/MM calculations were



performed using the MoFe QM/MM model. All QM/MM calculations were performed with Chemshell<sup>44,45</sup> with an interface to ORCA<sup>46,47</sup> version 4.2.1 (QM program) and DL\_POLY<sup>48</sup> (MM program). MM calculations used the CHARMM36 (ref. 49) force-field. All QM calculations employed the TPSSh density functional,<sup>50,51</sup> with D3BJ dispersion correction<sup>52,53</sup> and with the ZORA scalar relativistic approximation.<sup>54,55</sup> The relativistically recontracted ZORA-def2 basis set family was used (ZORA-def2-TZVP on Mo, V, Fe, S and carbide and ZORA-def2-SVP on other atoms).<sup>56,57</sup> The RIJCOSX approximation<sup>58,59</sup> for Coulomb and HF exchange integrals was used with a decontracted auxiliary basis set.<sup>60</sup> The QM/MM coupling was described using electrostatic embedding together with link atoms and a charge-shifting scheme.<sup>44</sup> QM/MM geometry optimizations used the DL-FIND program.<sup>61</sup> QM-regions of varying sizes were tested for FeMoco as well as different sized partial Hessians. In the case of  $[\text{Fe}_4\text{S}_4(\text{SPh})_4]^{2-}$  and for QM-cluster calculations of FeMoco, CPCM<sup>62</sup> was used as a continuum solvation model, with  $\epsilon = 4$  for FeMoco (simulating a protein environment) and  $\epsilon = \infty$  for  $[\text{Fe}_4\text{S}_4(\text{SPh})_4]^{2-}$  (simulating a polar crystal). The ZORA-TPSSh electronic structure level of theory has previously been shown to well-reproduce the geometries (M-Fe distances and M-S bond lengths) of spin-coupled iron-sulfur dimers and the high-resolution X-ray crystal structure of FeMoco.<sup>63,64</sup> Vibrational frequencies were calculated using a numerical one-point formula partial Hessian approach (of varying size) for QM/MM and numerical two-point formula QM-cluster calculations; a comparison of numerical one-point vs. two-point partial Hessian approaches for FeMoco is provided in Fig. S1.<sup>†</sup>  $^{57}\text{Fe}$  normal mode composition factors were calculated and used to derive  $^{57}\text{Fe}$  PVDOS. Each calculated vibrational transition was broadened by a  $12\text{ cm}^{-1}$  Gaussian (FWHM).

Broken-symmetry states for the FeMoco clusters, Mo N<sub>2</sub>ase P-cluster and  $[\text{Fe}_4\text{S}_4(\text{SPh})_4]^{2-}$  were found using a high-spin ferromagnetic initial state. The geometry for each BS state was optimized and the Hessian calculated. For FeMoco and FeVco, 3 different determinants of the favorable BS7 class were found as previously described:<sup>42,43,65,66</sup> BS7-235, BS7-346 and BS7-247 where the last 3 numbers refer to which Fe ions (X-ray structure numbering, Fig. S2<sup>†</sup>)<sup>67</sup> are spin-down. A total charge of  $n = -1$  was used when treating the total valency of FeMoco. As recent studies have suggested, extractions of VFe are comprised of a mixture of both EPR-active/catalytically inactive and EPR-silent/catalytically active components,<sup>21</sup> FeVco cluster charges ( $[\text{V-7Fe-8S-C-CO}_3]^{n-}$ ) with  $n = -2$  and  $-1$  were calculated in spin states of  $M_S = 3/2$  and  $M_S = 1$ , respectively, with a BS7-235 determinant, previously shown to be lowest in energy for FeVco.<sup>43</sup> For FeFeco, no X-ray structure has been reported in the literature and the redox state is not well established. Models using a  $[\text{8Fe-9S-C}]^n$  form with  $n = -2, -1, 0$  with  $M_S = 0, 1/2$ , and 1 spin states with a BS-0235 broken-symmetry determinant were calculated (where the 4 numbers refer to which Fe ions are spin-down, X-ray structure numbering as shown in Fig. S2<sup>†</sup>). For the P-cluster, an  $M_S = 0$  BS-1247 determinant was employed.

## Results and discussion

### NRVS of Mo N<sub>2</sub>ase

The  $^{57}\text{Fe}$ -enriched holo-MoFe protein from *Azotobacter vinelandii* contains two distinct metalloclusters, the P-cluster (8Fe-7S) and FeMoco ( $[\text{Mo-7Fe-9S-C-homocitrate}]$ ). A *ΔnifB* strain of *A. vinelandii* was used to produce apo-MoFe, ergo containing the  $^{57}\text{Fe}$ -enriched [8Fe-7S] P-cluster while lacking FeMoco. The



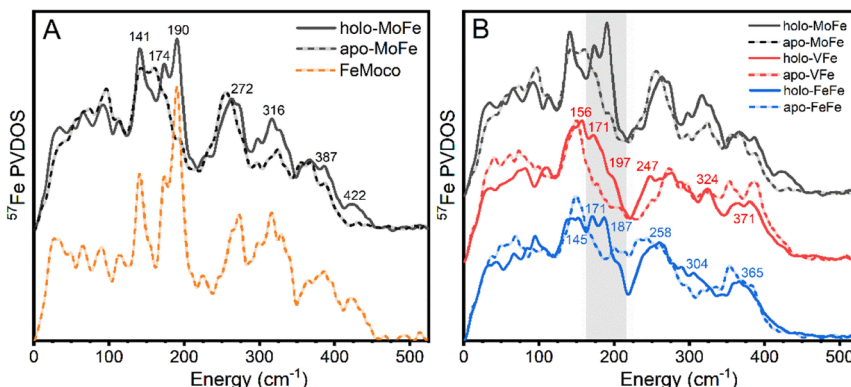


**Fig. 2** (A) Comparison of experimental  $^{57}\text{Fe}$  PVDOS of apo-MoFe (dashed, black) and holo-MoFe (solid, black). Additionally, the derived PVDOS of FeMoco is shown as an offset dashed orange line. (B) Comparison of the experimental  $^{57}\text{Fe}$  PVDOS of the three MFe proteins, in the holo- (solid lines) and the apo-forms (dashed lines). The shaded grey box indicates the primary distinct “FeMoco” contribution region. Displayed numbers refer to outstanding features of the holo PVDOS, and carry the unit  $\text{cm}^{-1}$ .

NRVS-derived  $^{57}\text{Fe}$  PVDOS of each apo-MoFe (corresponding to 8 unique Fe) and holo-MoFe (corresponding to 15 unique Fe) are presented in Fig. 2A. Additionally, the PVDOS of FeMoco, derived from the  $[\text{holo-MoFe}] - (8/15) \times [\text{apo-MoFe}]$  difference spectrum is also shown.

The  $^{57}\text{Fe}$  PVDOS of holo-MoFe protein exhibits a set of intense characteristic vibrational bands around 141, 174, 190, 272, 316, 387, and  $422\text{ cm}^{-1}$ . These vibrational frequencies match well with the previously reported PVDOS of Mo N<sub>2</sub>ase – a comparison is provided in Fig. S3.†<sup>32,33</sup> Similarly, the PVDOS of apo-MoFe (P-cluster only) also compares well with that previously reported, exhibiting relatively broad features  $\sim 155$ , 255, 323, and  $363\text{ cm}^{-1}$ . The broadness of these features likely arises from the relatively low symmetry of the P-cluster, leading to distributions of concerted bending and stretching modes. By subtracting the apo-MoFe spectrum from the holo-MoFe spectrum, a FeMoco-only spectrum can be obtained (PVDOS shown as orange dashed line, Fig. 2A) which has several clear fingerprints and allows the differences between the apo and holo protein to be more clearly highlighted. Well-resolved features appear on top of the broad bands arising from apo-MoFe, specifically  $\sim 140$  and  $270\text{ cm}^{-1}$ , while features at 190 and  $422\text{ cm}^{-1}$  appear as completely unique fingerprints to FeMoco. Additionally, a significant increase in intensity is observed for a series of features at  $\sim 320$  and  $390\text{ cm}^{-1}$ . Previous NRVS studies of  $[\text{Fe}_4\text{S}_4(\text{SPh})_4]^{2-}$  support assignment of the feature at  $\sim 140\text{ cm}^{-1}$  as a S-Fe-S bending vibration, while those at  $267$  and  $290\text{ cm}^{-1}$  likely arise from a series of Fe-S stretching modes (Fig. S4†).<sup>68</sup> Previously, the band appearing at  $\sim 190\text{ cm}^{-1}$  was assigned as a symmetric Fe<sub>6</sub>C stretch referred to as a “breathing” mode of the FeMoco cluster.<sup>32</sup> Meanwhile, the feature at  $422\text{ cm}^{-1}$  has not been explicitly assigned.

### NRVS of VFe and FeFe

To compare the vibrational features of the alternative N<sub>2</sub>ases with Mo N<sub>2</sub>ase, NRVS spectra of  $^{57}\text{Fe}$ -enriched samples of VFe and FeFe proteins in both holo- and



the apo-forms (lacking FeVco and FeFeco, respectively) were obtained, which are shown as the derived  $^{57}\text{Fe}$  PVDOS in Fig. 2B. Significant vibrational bands appear around 156, 171, 197 (as a shoulder), 247, 324, and  $371\text{ cm}^{-1}$  in holo-VFe. In apo-VFe, a primary feature  $\sim 149\text{ cm}^{-1}$  is observed, along with several features spanning the Fe-S stretching regime, particularly at 272, 295, 319, 353, and  $386\text{ cm}^{-1}$ . Similar to apo-MoFe, apo-VFe lacks significant spectral contributions in the range of  $170\text{--}240\text{ cm}^{-1}$ ; however, unlike apo-MoFe, spectral features in the  $\sim 270\text{ cm}^{-1}$  regime of apo-VFe are significantly less intense, leading to a broad energetic distribution. Comparing holo- and apo-VFe, we see that the energetic ranges from  $170\text{--}200\text{ cm}^{-1}$  and  $\sim 250\text{ cm}^{-1}$  appear to be unique to the holo protein.

In holo-FeFe, significant features appear around 143, 171, 187, 258, 304, and  $365\text{ cm}^{-1}$ , while the apo-FeFe PVDOS exhibits a distinct feature at  $147\text{ cm}^{-1}$ , along with very broad bands in the  $200\text{--}340$  range, and several distinct peaks at 354 and  $383\text{ cm}^{-1}$ . Like apo-MoFe and apo-VFe, the appearance of a significant band  $\sim 150\text{ cm}^{-1}$  makes this a distinct feature common to the P-clusters of all three N<sub>2</sub>ases. However, unlike apo-MoFe and apo-VFe, significant intensity is still observed in the  $200\text{--}250\text{ cm}^{-1}$  region of apo-FeFe, making the PVDOS of this protein particularly distinct from both apo-MoFe and apo-FeFe.

Comparing the PVDOS of MoFe, VFe, and FeFe together, several commonalities and differences become readily apparent. All three holo-proteins exhibit increased intensity in the  $170\text{--}210\text{ cm}^{-1}$  region relative to their apo-forms, supporting that this region provides a strong, common fingerprint for all three FeM-cofactors. However, the bulk of intensity for this region is shifted to lower energy in holo-VFe relative to either holo-MoFe or FeFe. One notable difference between holo-MoFe and either VFe or FeFe is a distinct lack of the high-energy feature  $\sim 422\text{ cm}^{-1}$  in the latter, implying a structural shift between MoFe and either VFe or FeFe.

Based on the reported high-resolution crystal structures of MoFe<sup>8</sup> and VFe,<sup>9</sup> we anticipated the P-clusters of apo-MoFe and apo-VFe (and by extension, apo-FeFe) to appear near-identical. However, we observe major discrepancies between the three apo-N<sub>2</sub>ase PVDOS. While these differences may arise from the unique protein environment-induced modulation of the P-cluster in each enzyme, we caution that the risk of sample heterogeneity due to the one-step affinity purification technique used for sample preparation cannot be ruled out. This technique is commonly employed and allows for fast sample preparation; however, it acts as a double-edged sword. Rapid purification significantly reduces the risk of protein denaturation and metallocluster damage, while simultaneously carrying the risk that a distribution of nitrogenase complexes in different maturation states may be present in the purified product. In MoFe isolated from wild-type *A. vinelandii* cells *via* one-step affinity purification, both the P-cluster and FeMoco are fully matured;<sup>69,70</sup> however, it is not yet established if this is the case for VFe and FeFe purified when the same technique is applied, and specifically to how these compositions may vary between strains producing apo- vs. holo-VFe and FeFe. Moreover, the properties of the P-cluster in VFe and FeFe are not yet fully understood; notably, our EPR measurements of holo- and apo-VFe display a significant  $S = 1/2$  signal, which may be tentatively attributed to either damaged P-cluster, a maturation intermediate, or even both (Fig. S5†).<sup>21,71</sup> A similar signal has also been observed in the EPR spectrum of FeFe, as well as in the present study.<sup>26</sup> A detailed investigation is currently underway in our lab to further



understand these differences. Nevertheless, amid these cautions, we emphasize that there are general differences between all apo and holo proteins which allow us to clearly assign spectral regions that are dominated by FeMco cluster contributions.

### Calculations of $[\text{Fe}_4\text{S}_4(\text{SPh})_4]^{2-}$ , P-cluster, and FeMco NRVS

Calculations of the  $^{57}\text{Fe}$  PVDOS require only the calculation of a mass-weighted Hessian matrix that can be obtained at the QM or QM/MM level of theory *via* the harmonic approximation. The harmonic vibrational energies come directly from the normal mode analysis as do the intensities ( $^{57}\text{Fe}$  normal mode composition factors). A previous NRVS experiment on a [4Fe-4S] cubane cluster with (SPh) ligation ( $[\text{Fe}_4\text{S}_4(\text{SPh})_4]^{2-}$ ) was found to serve a useful purpose for calibration.<sup>68</sup> More specifically, it shares some of the same basic structural features as the FeMco clusters, having weak-field tetrahedral Fe sites in  $\text{Fe}^{\text{II}}/\text{Fe}^{\text{III}}$  oxidation states with a mixed-valence delocalized electronic structure and containing both inorganic  $\mu^3$ -sulfides and thiolates, while lacking a carbide and  $\mu^2$ -sulfides. The experimental PVDOS shown in Fig. 3 reveals NRVS intensity in most parts of the spectrum across the 0–400  $\text{cm}^{-1}$  region, though notably lacking significant intensity at  $\sim 190 \text{ cm}^{-1}$ .

As Fig. 3 also reveals, the calculated PVDOS of  $[\text{Fe}_4\text{S}_4(\text{SPh})_4]^{2-}$  (modeled as a simple dianionic cluster surrounded by a polarizable continuum) can reproduce the main peaks in the experimental PVDOS well, demonstrating the applicability of the electronic structure approach (ZORA-TPSSh). No signs of systematic overestimation are indicated, and thus no empirical scaling factor has been introduced. According to the calculations, the 330–430  $\text{cm}^{-1}$  region consists of Fe–S

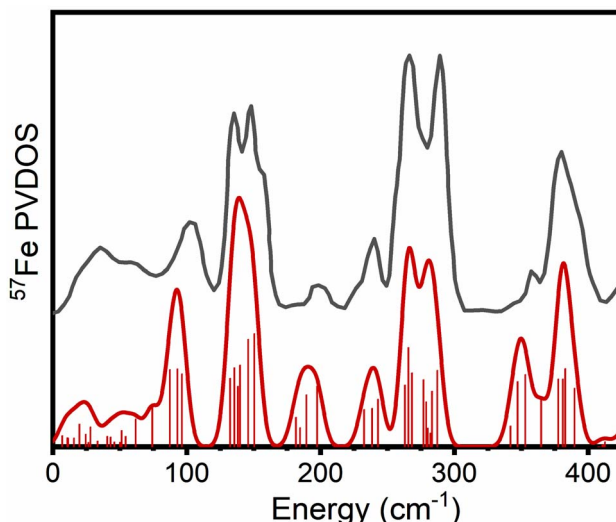


Fig. 3 Calculated PVDOS of  $[\text{Fe}_4\text{S}_4(\text{SPh})_4]^{2-}$  (red) vs. experimental PVDOS of  $[(n\text{-Bu})_4\text{N}]_2[\text{Fe}_4\text{S}_4(\text{SPh})_4]$  (dark grey). Individual calculated modes and their intensities are represented as bars, while the solid line represents the 12  $\text{cm}^{-1}$  FWHM broadened composite PVDOS. The experimental PVDOS of  $[(n\text{-Bu})_4\text{N}]_2[\text{Fe}_4\text{S}_4(\text{SPh})_4]$  has been adapted from ref. 68 with permission from the Royal Society of Chemistry.



stretching modes, involving both  $\mu^3$ -sulfides and thiolates, some of them strongly coupled. The 200–300  $\text{cm}^{-1}$  region consists of various types of bending modes with some Fe-S stretching character while the 90–150  $\text{cm}^{-1}$  region primarily contains bending modes with much less Fe-S stretching character. The ESI<sup>†</sup> contains animations of vibrational modes with substantial iron contributions.

The apo-MoFe PVDOS should consist solely of the contribution of the P-cluster. The P-cluster, an [8Fe-7S] cluster, can be envisioned as a fusion of 2 [4Fe-4S] cubanes at a corner through an interstitial sulphide. While there are clear similarities between the [4Fe-4S] cubane PVDOS in Fig. 3 and the P-cluster PVDOS presented in Fig. 4A (intensity at  $\sim 140$ ,  $\sim 270$  and  $380 \text{ cm}^{-1}$ ), the P-cluster also gives rise to a broader spectral envelope, as would be expected from the more complex molecular structure, featuring both terminal and bridging thiolates,  $\mu^3$ -sulfides in distorted cubanes and an unusual  $\mu^6$ -sulfide. Visualization of the calculated vibrational modes reveal considerable complexity. Briefly, the 300–400  $\text{cm}^{-1}$  region contains Fe-S stretching modes involving  $\mu^3$ -sulfides (346–426  $\text{cm}^{-1}$ ) and thiolates (309–345  $\text{cm}^{-1}$ ). Stretching modes involving the  $\mu^6$ -sulfide appear at 275–293  $\text{cm}^{-1}$ . Most of the individual stretching modes are localized to each sub-cubane of the P-cluster, however, some are delocalized over the whole cluster. The region of 120–270  $\text{cm}^{-1}$  consists primarily of various bending modes (higher energy ones having some stretching thiolate character) that are delocalized over the whole cluster. Despite the additional complexity that arises in the P-cluster and the complex coupled nature of most of the modes (see ESI<sup>†</sup> for animations), the QM/MM calculation of MoFe protein with the P-cluster in the QM-region is reassuringly able to reproduce the main PVDOS features of the spectrum quite well.

The FeMoco cluster of nitrogenase can also be approximately described as a fusion of two cubanes (e.g. [4Fe-4S] and [Mo-3Fe-4S]) but, importantly, contains an interstitial carbide that makes this cluster structurally distinct. The sensitivity

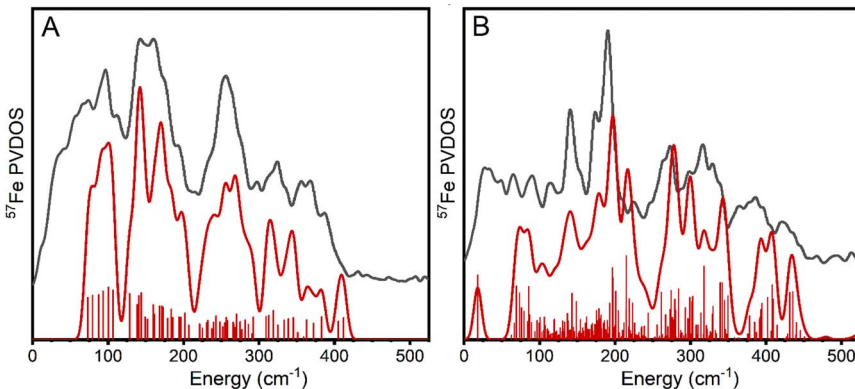


**Fig. 4** (A) Calculated P-cluster PVDOS from the MoFe QM/MM model, BS-1247, (red line) compared to the experimental apo-MoFe PVDOS (black). Calculations were performed using a 39 atom QM-region/Hessian. (B) Overlay of calculated FeMoco (red, solid) vs. derived experimental FeMoco (black, solid) PVDOS. Individual calculated modes and their intensities are represented as bars, while the solid line represents the  $12 \text{ cm}^{-1}$  FWHM broadened composite PVDOS. Calculations were performed considering 247 atoms in the QM-region/Hessian and a BS7-235 broken-symmetry solution.



of the calculated PVDOS of the FeMoco system was tested with respect to several calculation variables, including cluster-model *vs.* QM/MM, QM/MM with varying QM-region and partial Hessian sizes, and different broken-symmetry solutions. Overall, the use of QM/MM, rather than cluster model, is found to be critical (Fig. S6 of the ESI†) and while there is some sensitivity with respect to QM-region and size of partial Hessian, a small QM-region and Hessian region reproduces the main features of the largest calculation well (Fig. S7†). Furthermore, observed spectral improvements (compared to experiment) appear to arise more-so from a systematic improvement in geometry accuracy rather than the increased size of the partial Hessian.

Overall, the experimental PVDOS is well reproduced by QM/MM calculations (Fig. 4B), with the primary deviations being a lack of calculated intensity in the 360–370  $\text{cm}^{-1}$  region (likely due to an overestimation of the calculated modes 380–440  $\text{cm}^{-1}$  by 10–20  $\text{cm}^{-1}$ ) and the appearance of an additional peak in the 200–210  $\text{cm}^{-1}$  region. As mentioned earlier, the 170–210  $\text{cm}^{-1}$  region appears particularly unique to FeMoco. Previous analysis of calculated PVDOS by Cramer and co-workers have described this region as arising from an  $\text{Fe}_6\text{X}$  ( $\text{X} = \text{C, N, O}$ ) “breathing” mode,<sup>32</sup> where the relatively high energy (190  $\text{cm}^{-1}$  *vs.* 150  $\text{cm}^{-1}$  as seen in other cubanes<sup>68</sup>) arises from the additional cluster rigidity conferred by the central atom. Our present analysis reveals an important reason why this region of the MoFe PVDOS is FeMoco-specific: the modes involve Fe–carbide stretching character. More precisely, the modes in this region involve a pair of Fe ions in each sub-cubane (Fe2–Fe6, Fe3–Fe7 and Fe4–Fe5) and can be described as a combination of anti-symmetric Fe–carbide stretching modes and bridging belt sulphide wagging, both being structural properties unique to the FeMoco cluster in MoFe. Calculated modes are available for visualization in the ESI.†

Closer inspection of the additional calculated peak in the 200–210  $\text{cm}^{-1}$  region reveals that it maintains very similar character to those modes at 170–200  $\text{cm}^{-1}$ , with each having dominant Fe–carbide stretching character involving a pair of belt Fe ions. The reason for the higher-energy shift of the modes to 200–210  $\text{cm}^{-1}$  arises from the additional involvement of the Fe4–Fe5 pair. In the specific broken-symmetry solution calculated, BS7-235, Fe4–Fe5 is best described as a pair of ferric Fe ions (with the other Fe ions being mixed-valence delocalized), as previously described.<sup>42</sup> The difference in Fe oxidation state in the BS-state calculated thus offers an explanation for the appearance of the higher energy peak in the calculated PVDOS. There are two plausible explanations for why this occurs in our calculations: (i) our choice of density functional (TPSSh) overestimates the effective Fe oxidation state differences (*i.e.*, the covalency is not captured well enough) and/or (ii) the broken-symmetry approach lacks the flexibility to fully describe the electronic structure.

Regarding density functional choice, we note that our electronic structure protocol has been previously shown to reproduce the high-resolution X-ray structure of FeMoco and related spin-coupled dimers very well,<sup>42,63</sup> likely due to a balanced treatment of covalency in the Fe–S bonds. However, less is known about the quality of the electronic structure description regarding the Fe–carbide bonds, and any over/under estimation of Fe–C covalency may well lead to the observed deviations in the 170–200  $\text{cm}^{-1}$  region.

Another plausible explanation arises from the implementation of spin-symmetry broken DFT. In particular, we find that a single determinant (BS7-



235) leads to this additional calculated peak. There are 3 BS7 determinants (BS7-235, BS7-346 and BS7-247) that are effectively energetically equivalent at the TPSSh-level of theory ( $\sim 1$  kcal mol $^{-1}$  energy difference). These 3 determinants give rise to distinct geometric FeMoco structures which can be interpreted as 3 distinct electronic states, with BS7-235 providing the best agreement with the high-resolution X-ray structure. Alternatively, the true wavefunction of FeMoco could be conceived as a combination of these 3 determinants. As shown in Fig. S8,<sup>†</sup> calculating the PVDOS for each BS determinant leads to non-negligible changes (a direct result of the distinct geometries), including in the 190–210 cm $^{-1}$  region. It is possible that the failure of our electronic structure protocol to fully describe this spectral region could be a result of the limitation of the BS-DFT approach, perhaps necessitating a weighted average of calculated PVDOS over all 3 determinants. These results thus serve as inspiration for improving the electronic structure description of FeMoco, which is currently limited to broken-symmetry DFT.

Finally, we turn to a comparison of the QM/MM calculated PVDOS for FeMoco, FeVco and FeFeco; as a crystallographic structure of FeFeco has not yet been reported, the protein environment of MoFe was employed in the case of the FeFe protein. For FeVco, both the  $[V\text{-}7\text{Fe}\text{-}8\text{S}\text{-}\text{C}\text{-}\text{CO}_3]^{2-}$  and  $[V\text{-}7\text{Fe}\text{-}8\text{S}\text{-}\text{C}\text{-}\text{CO}_3]^-$  redox states were calculated. Previous QM/MM calculations have shown that the  $[V\text{-}7\text{Fe}\text{-}8\text{S}\text{-}\text{C}\text{-}\text{CO}_3]^{2-}$  redox state ( $M_S = 3/2$ ) provides the best calculated structural agreement with the VFe protein X-ray structure<sup>43</sup> (which may not be the resting state) while remaining consistent with the  $S = 3/2$  EPR signal previously attributed to the VFe resting state. However, recent EPR studies have suggested that the resting state of active FeVco is actually EPR-silent, wherein the  $S = 1/2$  EPR signal originates from the P-cluster or P-cluster maturation intermediates, while the two  $S = 3/2$  signals are associated with inactive forms of FeVco.<sup>21</sup> The redox state of FeFeco is also not confidently known, and a valency of  $[8\text{Fe}\text{-}9\text{S}\text{-}\text{C}]^{2-}$  has been presently employed, as shown in Fig. 5; the calculated PVDOS for alternative redox state possibilities ( $[8\text{Fe}\text{-}9\text{S}\text{-}\text{C}]^-$  and  $[8\text{Fe}\text{-}9\text{S}\text{-}\text{C}]^0$ ) are provided in the ESI (Fig. S9<sup>†</sup>).

Similar to our experimental observations, comparisons of QM/MM Hessian calculations of FeMoco, FeVco, and FeFeco reveal that structural differences of the cofactors translate into considerably different PVDOS. However, there is a closer correspondence between the PVDOS of FeMoco and FeFeco, with FeVco clearly being the most different of the three (regardless of redox state calculated). In particular, the region ranging from 170–210 cm $^{-1}$  differs considerably for FeVco, likely due to the substitution of a belt sulphide for carbonate in FeVco, which would be expected to shift the energy of the modes in this region. There is also a sensitivity to which FeVco redox state is calculated; however, it remains unclear which spectrum is in better agreement with experiment. In the observed experimental PVDOS of VFe, the dominant intensity of this region is red-shifted to  $\sim 170$  cm $^{-1}$  (as compared to  $\sim 190$  cm $^{-1}$  in MoFe and FeFe). The observed variations within the 170–210 cm $^{-1}$  region, combined with the (a) crystallographically demonstrated differences in belt atom identity and (b) high similarity of the PVDOS of FeFe and MoFe in this region supports the presence of three belt-sulphurs in the resting state of FeFeco.

The highest energy experimental feature at 422 cm $^{-1}$  in the PVDOS of FeMoco presented in Fig. 4B is well reproduced by our QM/MM calculations ( $\sim 440$  cm $^{-1}$ ), and is plausibly assigned to an Fe-S stretching mode involving the belt sulphide



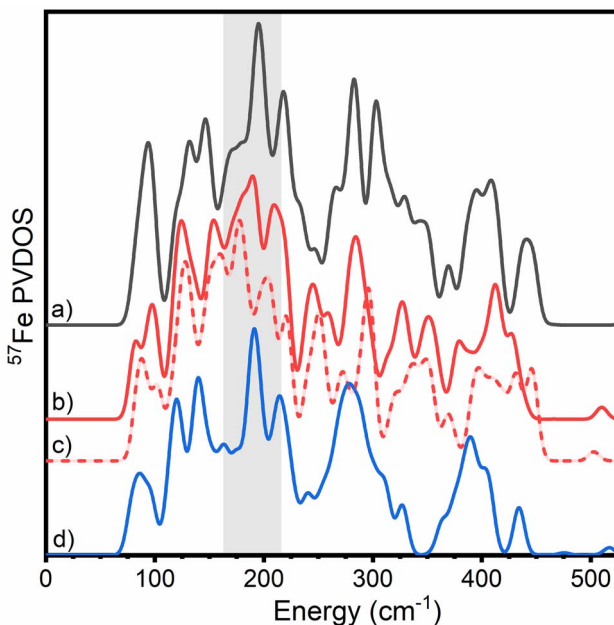


**Fig. 5** Overlay of calculated PVDOS of all three nitrogenase FeM-cofactors according to QM/MM calculations. (a) FeMoco ( $[\text{Mo}-7\text{Fe}-9\text{S}-\text{C}]^-$ ,  $M_S = 3/2$ , BS7-235) (black), (b) FeVco ( $[\text{V}-7\text{Fe}-8\text{S}-\text{C}-\text{CO}_3]^{2-}$ ,  $M_S = 3/2$ , BS7-235) (red, solid), (c) ( $[\text{V}-7\text{Fe}-8\text{S}-\text{C}-\text{CO}_3]^-$ ,  $M_S = 1$ , BS7-235) (red, dashed) and (d) FeFeco ( $[\text{8Fe}-9\text{S}-\text{C}]^{2-}$ ,  $M_S = 0$ , BS7-235) (blue). Calculations were carried out with 54 atoms in QM/Hessian region for FeMoco and FeFeco, and 57 atoms in QM/Hessian region for FeVco. Calculations of FeFeco employed a MoFe-based secondary coordination sphere. The region of interest described for the experimental  $\text{N}_2\text{ase}$  PVDOS in Fig. 2 is highlighted in grey.

of FeMoco, specifically the S2B sulphide bridging  $\text{Fe}_2$  and  $\text{Fe}_6$  (see ESI† for animated modes). The analogous modes of belt sulphides S5A and S3A are calculated to be lower in energy ( $350-400\text{ cm}^{-1}$ ). The origin of the high-energy of this specific Fe-S belt sulphide stretching mode is likely related to the environment around S2B in MoFe, with a directional hydrogen bond donated from His195. As shown in Fig. S6,† the CPCM-cluster model (lacking an explicit protein environment) does not produce this high-energy feature. The lack of this high-energy feature in the experimental VFe and FeFe PVDOS, however, is more likely related to different resting redox states of the cofactor, which can shift the energy of the feature as shown in Fig. 5. Among the FeVco redox states calculated, the  $[\text{V}-7\text{Fe}-8\text{S}-\text{C}-\text{CO}_3]^{2-}$  calculation is found to be more consistent with experiment (*i.e.*, lacking a high-energy feature relative to FeMoco) than the  $[\text{V}-7\text{Fe}-8\text{S}-\text{C}-\text{CO}_3]^-$  calculation. As shown in Fig. S9,† the  $[\text{8Fe}-9\text{S}-\text{C}]^{2-}$  redox state appears to be in better agreement with experiment than either  $[\text{8Fe}-9\text{S}-\text{C}]^-$  or  $[\text{8Fe}-9\text{S}-\text{C}]^0$ .

## Recommendations and concluding remarks

Herein, we have presented a comparison of the NRVS data for all three forms of nitrogenase enzymes in both their holo and apo forms. The experimental data



display distinct spectral features which can be correlated to contributions from the FeMco clusters in the 170–210 cm<sup>−1</sup> region. The three holo protein PVDOS show subtle variations in this spectral region, with MoFe and FeFe being more similar to each other than VFe. In addition, holo MoFe shows a unique feature at 422 cm<sup>−1</sup>, which is absent in the other two holo proteins.

Using DFT-based QM/MM calculations, we were able to obtain further insight into the origins of these spectral features. Our calculations have shown that both a simple 4Fe-4S model complex, as well as the P-cluster NRVS data can be well modelled using our BS-DFT based approach. Both the experimental data and calculations show the evolution of spectral complexity moving from a 4Fe-4S cubane to the P-cluster, and finally to the FeMco clusters. While the 4Fe-4S cluster and the P-clusters of MoFe protein are generally well reproduced by our calculations, modelling the FeMco clusters in terms of both valency and spin state shows greater variability. Specifically, for FeMoco, we have observed that the calculated PVDOS are very sensitive to the computational modelling protocol employed. It is clear that a QM/MM model, rather than a cluster model, is required to accurately capture primary spectral features. For instance, the clear band observed experimentally at ~420 cm<sup>−1</sup> is only reproduced computationally in the QM/MM model, demonstrating the importance of properly modelling the protein environment. We note that this feature is unique to FeMoco, and can be attributed to an Fe-S2B stretching mode. The identification of this feature is of great interest as the S2B position is thought to be potentially labile during catalysis.<sup>19,24,72–74</sup> This assignment hence provides a spectroscopic signature for identifying its contributions, which may be of great utility in future studies of MoFe intermediates.

Our calculations have proven to be less sensitive to the size of the QM region, indicating that relatively small QM regions may represent a reasonable convergence of the Hessian. However, these calculations are also sensitive to the specific (almost isoenergetic) broken symmetry determinant used in the electronic structure calculations of FeMoco, particularly in the 170–210 cm<sup>−1</sup> region. Presently, this dependence is not completely understood but may indicate that averaging over multiple broken symmetry determinants is necessary to fully capture the distinct experimental peak patterns of this region. The present findings thus further demonstrate the need to develop computational approaches that go beyond BS-DFT. Here, recent developments in wave function-based *ab initio* approaches to iron–sulphur clusters and to nitrogenase clusters are of great interest.<sup>75–77</sup>

The issues discussed here become even more complex for FeVco, where the ground state electronic structure remains a subject of debate.<sup>21</sup> For FeFeco, the complexity is even further increased due to our present lack of understanding regarding the ground state electronic structure and the fact that a crystal structure is not currently available in the literature. In spite of these limitations, we are able to qualitatively capture the trends observed in our experimental data. We note, however, that these results highlight that caution must be exercised in using calculated PVDOS to quantitatively evaluate changes in the experimental PVDOS. In particular, using the discrete frequency of an observed feature to assign a given geometric/electronic structure state may be treacherous.

Finally, in closing, we note that these findings also have broad implications for the use of DFT cluster models to simulate the NRVS for many other metalloprotein



systems. Specifically, the observations herein indicate that the failure to properly model the H-bonding from the protein environment may result not only in spectral shifts, but potentially even in the absence of certain spectral features. This provides an important cautionary note for the application of overly simplistic cluster models to calculate metalloprotein PVDOS – particularly in cases where open geometric and electronic structure questions may complicate the modelling.

## Author contributions

CVS, RB and SD planned and designed the study. Expression and purification of nitrogenases was performed by LD, and sample preparation was performed by CVS and LD. Beamtime data collection was carried out by CVS, YY, DB and AC. Data analysis was carried out by CVS, AR, and SD. Computational studies were performed by BB under the guidance of RB. The manuscript was written by CVS, BB, AR, LD, RB, SD, and edited by all authors.

## Conflicts of interest

There are no conflicts to declare.

## Acknowledgements

We gratefully thank Prof. Dennis Dean and Valerie Cash (Virginia Polytechnic Institute and State University, USA) for providing the *A. vinelandii* strains used for this work. The authors acknowledge the Max Planck Society for funding. Additionally, SD and CVS acknowledge the DFG SPP 1927 “Iron–Sulfur for Life” (Project DE 1877/1-2 (SD)) for funding. Synchrotron radiation experiments at SPring-8 BL19LXU were performed with the approval of the Japan Synchrotron Radiation Research Institute (JASRI) (Proposal. Nos. 2019A1700, 2020A1413). Experiments were performed in part at beamline ID18 of the European Synchrotron Radiation Facility (ESRF), Grenoble, France. BB acknowledges support from the Teacher Assistant Grant of the University of Iceland. Open Access funding provided by the Max Planck Society. A. R. thanks the Alexander von Humboldt Foundation for a postdoctoral fellowship.

## Notes and references

- 1 X. Zhang, B. B. Ward and D. M. Sigman, *Chem. Rev.*, 2020, **120**, 5308–5351.
- 2 D. Fowler, M. Coyle, U. Skiba, M. A. Sutton, J. N. Cape, S. Reis, L. J. Sheppard, A. Jenkins, B. Grizzetti, J. N. Galloway, P. Vitousek, A. Leach, A. F. Bouwman, K. Butterbach-Bahl, F. Dentener, D. Stevenson, M. Amann and M. Voss, *Philos. Trans. R. Soc., B*, 2013, **368**, 20130164.
- 3 F. Haber, *Naturwissenschaften*, 1922, **10**, 1041–1049.
- 4 G. J. Leigh, in *Catalysts for Nitrogen Fixation: Nitrogenases, Relevant Chemical Models and Commercial Processes*, ed. B. E. Smith, R. L. Richards and W. E. Newton, Springer Netherlands, Dordrecht, 2004, pp. 33–54.
- 5 S. T. Stripp, B. R. Duffus, V. Fourmond, C. Léger, S. Leimkühler, S. Hirota, Y. Hu, A. Jasniewski, H. Ogata and M. W. Ribbe, *Chem. Rev.*, 2022, **122**, 11900–11973.



6 B. K. Burgess and D. J. Lowe, *Chem. Rev.*, 1996, **96**, 2983–3012.

7 L. C. Seefeldt, Z.-Y. Yang, D. A. Lukyanov, D. F. Harris, D. R. Dean, S. Raugei and B. M. Hoffman, *Chem. Rev.*, 2020, **120**, 5082–5106.

8 T. Spatzl, M. Aksoyoglu, L. Zhang, S. L. A. Andrade, E. Schleicher, S. Weber, D. C. Rees and O. Einsle, *Science*, 2011, **334**, 940.

9 D. Sippel and O. Einsle, *Nat. Chem. Biol.*, 2017, **13**, 956–960.

10 M. Varadi, S. Anyango, M. Deshpande, S. Nair, C. Natassia, G. Yordanova, D. Yuan, O. Stroe, G. Wood, A. Laydon, A. Žídek, T. Green, K. Tunyasuvunakool, S. Petersen, J. Jumper, E. Clancy, R. Green, A. Vora, M. Lutfi, M. Figurnov, A. Cowie, N. Hobbs, P. Kohli, G. Kleywegt, E. Birney, D. Hassabis and S. Velankar, *Nucleic Acids Res.*, 2022, **50**, D439–D444.

11 J. C. Setubal, P. dos Santos, B. S. Goldman, H. Ertesvag, G. Espin, L. M. Rubio, S. Valla, N. F. Almeida, D. Balasubramanian, L. Cromes, L. Curatti, Z. Du, E. Godsy, B. Goodner, K. Hellner-Burris, J. A. Hernandez, K. Houmiel, J. Imperial, C. Kennedy, T. J. Larson, P. Latreille, L. S. Ligon, J. Lu, M. Maerk, N. M. Miller, S. Norton, I. P. O'Carroll, I. Paulsen, E. C. Raulfs, R. Roemer, J. Rosser, D. Segura, S. Slater, S. L. Stricklin, D. J. Studholme, J. Sun, C. J. Viana, E. Wallin, B. Wang, C. Wheeler, H. Zhu, D. R. Dean, R. Dixon and D. Wood, *J. Bacteriol.*, 2009, **191**, 4534–4545.

12 H. L. Rutledge and F. A. Tezcan, *Chem. Rev.*, 2020, **120**, 5158–5193.

13 E. Krahn, B. Weiss, M. Kröckel, J. Groppe, G. Henkel, S. Cramer, A. Trautwein, K. Schneider and A. Müller, *JBIC, J. Biol. Inorg. Chem.*, 2002, **7**, 37–45.

14 C. Van Stappen, L. Decamps, G. E. Cutsail, III, R. Bjornsson, J. T. Henthorn, J. A. Birrell and S. DeBeer, *Chem. Rev.*, 2020, **120**, 5005–5081.

15 C. Van Stappen, R. Davydov, Z.-Y. Yang, R. Fan, Y. Guo, E. Bill, L. C. Seefeldt, B. M. Hoffman and S. DeBeer, *Inorg. Chem.*, 2019, **58**, 12365–12376.

16 J. T. Henthorn, R. J. Arias, S. Koroidov, T. Kroll, D. Sokaras, U. Bergmann, D. C. Rees and S. DeBeer, *J. Am. Chem. Soc.*, 2019, **141**, 13676–13688.

17 D. Lukyanov, B. M. Barney, D. R. Dean, L. C. Seefeldt and B. M. Hoffman, *Proc. Natl. Acad. Sci. U. S. A.*, 2007, **104**, 1451–1455.

18 S. Raugei, L. C. Seefeldt and B. M. Hoffman, *Proc. Natl. Acad. Sci. U. S. A.*, 2018, **115**, E10521–E10530.

19 C. Van Stappen, A. T. Thorhallsson, L. Decamps, R. Bjornsson and S. DeBeer, *Chem. Sci.*, 2019, **10**, 9807–9821.

20 B. M. Hoffman, D. Lukyanov, Z.-Y. Yang, D. R. Dean and L. C. Seefeldt, *Chem. Rev.*, 2014, **114**, 4041–4062.

21 Z.-Y. Yang, E. Jimenez-Vicente, H. Kallas, D. A. Lukyanov, H. Yang, J. S. Martin del Campo, D. R. Dean, B. M. Hoffman and L. C. Seefeldt, *Chem. Sci.*, 2021, **12**, 6913–6922.

22 M. Rohde, K. Grunau and O. Einsle, *Angew. Chem., Int. Ed.*, 2020, **59**, 23626–23630.

23 D. Sippel, M. Rohde, J. Netzer, C. Trncik, J. Gies, K. Grunau, I. Djurdjevic, L. Decamps, S. L. A. Andrade and O. Einsle, *Science*, 2018, **359**, 1484–1489.

24 M. Rohde, K. Laun, I. Zebger, S. T. Stripp and O. Einsle, *Sci. Adv.*, 2021, **7**, eabg4474.

25 J. A. Rees, R. Bjornsson, J. Schlesier, D. Sippel, O. Einsle and S. DeBeer, *Angew. Chem., Int. Ed.*, 2015, **54**, 13249–13252.

26 K. Schneider, U. Gollan, S. Selsemeier-Voigt, W. Plass and A. Muffler, *Naturwissenschaften*, 1994, **81**, 405–408.



27 D. A. Lukoyanov, D. F. Harris, Z. Y. Yang, A. Perez-Gonzalez, D. R. Dean, L. C. Seefeldt and B. M. Hoffman, *Inorg. Chem.*, 2022, **61**, 5459–5464.

28 L. Decamps, D. B. Rice and S. DeBeer, *Angew. Chem., Int. Ed.*, 2022, **61**, e202209190.

29 S. G. MacArdle and D. C. Rees, *J. Am. Chem. Soc.*, 2022, **144**, 21125–21135.

30 K. M. Lancaster, M. Roemelt, P. Ettenhuber, Y. Hu, M. W. Ribbe, F. Neese, U. Bergmann and S. DeBeer, *Science*, 2011, **334**, 974–977.

31 D. A. Lukoyanov, Z.-Y. Yang, A. Pérez-González, S. Raugei, D. R. Dean, L. C. Seefeldt and B. M. Hoffman, *J. Am. Chem. Soc.*, 2022, **144**, 18315–18328.

32 Y. Xiao, K. Fisher, M. C. Smith, W. E. Newton, D. A. Case, S. J. George, H. Wang, W. Sturhahn, E. E. Alp, J. Zhao, Y. Yoda and S. P. Cramer, *J. Am. Chem. Soc.*, 2006, **128**, 7608–7612.

33 A. D. Scott, V. Pelmenschikov, Y. Guo, L. Yan, H. Wang, S. J. George, C. H. Dapper, W. E. Newton, Y. Yoda, Y. Tanaka and S. P. Cramer, *J. Am. Chem. Soc.*, 2014, **136**, 15942–15954.

34 A. I. Chumakov, R. Rüffer, H. Grünsteudel, H. F. Grünsteudel, G. Grübel, J. Metge, O. Leupold and H. A. Goodwin, *Europhys. Lett.*, 1995, **30**, 427–432.

35 W. Sturhahn, T. S. Toellner, E. E. Alp, X. Zhang, M. Ando, Y. Yoda, S. Kikuta, M. Seto, C. W. Kimball and B. Dabrowski, *Phys. Rev. Lett.*, 1995, **74**, 3832–3835.

36 E. Jiménez-Vicente, J. S. Martin Del Campo, Z.-Y. Yang, V. L. Cash, D. R. Dean and L. C. Seefeldt, in *Methods in Enzymology*, ed. F. Armstrong, Academic Press, 2018, vol. 613, pp. 231–255.

37 D. F. Harris, E. Jimenez-Vicente, Z.-Y. Yang, B. M. Hoffman, D. R. Dean and L. C. Seefeldt, *J. Inorg. Biochem.*, 2020, **213**, 111278.

38 H. J. Lipkin, *Phys. Rev. B: Condens. Matter Mater. Phys.*, 1995, **52**, 10073–10079.

39 W. Sturhahn, *Hyperfine Interact.*, 2000, **125**, 149–172.

40 V. G. Kohn and A. I. Chumakov, *Hyperfine Interact.*, 2000, **125**, 205–221.

41 W. Dong, H. Wang, M. M. Olmstead, J. C. Fettinger, J. Nix, H. Uchiyama, S. Tsutsui, A. Q. R. Baron, E. Dowty and S. P. Cramer, *Inorg. Chem.*, 2013, **52**, 6767–6769.

42 B. Benediktsson and R. Bjornsson, *Inorg. Chem.*, 2017, **56**, 13417–13429.

43 B. Benediktsson and R. Bjornsson, *Inorg. Chem.*, 2020, **59**, 11514–11527.

44 P. Sherwood, A. H. de Vries, M. F. Guest, G. Schreckenbach, C. R. A. Catlow, S. A. French, A. A. Sokol, S. T. Bromley, W. Thiel, A. J. Turner, S. Billeter, F. Terstegen, S. Thiel, J. Kendrick, S. C. Rogers, J. Casci, M. Watson, F. King, E. Karlsen, M. Sjøvoll, A. Fahmi, A. Schäfer and C. Lennartz, *J. Mol. Struct.*, 2003, **632**, 1–28.

45 S. Metz, J. Kästner, A. A. Sokol, T. W. Keal and P. Sherwood, *Wiley Interdiscip. Rev.: Comput. Mol. Sci.*, 2014, **4**, 101–110.

46 F. Neese, *Wiley Interdiscip. Rev.: Comput. Mol. Sci.*, 2012, **2**, 73–78.

47 F. Neese, *Wiley Interdiscip. Rev.: Comput. Mol. Sci.*, 2018, **8**, e1327.

48 W. Smith and T. R. Forester, *J. Mol. Graphics*, 1996, **14**, 136–141.

49 R. B. Best, X. Zhu, J. Shim, P. E. M. Lopes, J. Mittal, M. Feig and A. D. MacKerell Jr, *J. Chem. Theory Comput.*, 2012, **8**, 3257–3273.

50 J. Tao, J. P. Perdew, V. N. Staroverov and G. E. Scuseria, *Phys. Rev. Lett.*, 2003, **91**, 146401.

51 V. N. Staroverov, G. E. Scuseria, J. Tao and J. P. Perdew, *J. Chem. Phys.*, 2003, **119**, 12129–12137.



52 S. Grimme, J. Antony, S. Ehrlich and H. Krieg, *J. Chem. Phys.*, 2010, **132**, 154104.

53 S. Grimme, S. Ehrlich and L. Goerigk, *J. Comput. Chem.*, 2011, **32**, 1456–1465.

54 E. van Lenthe, E. J. Baerends and J. G. Snijders, *J. Chem. Phys.*, 1993, **99**, 4597–4610.

55 C. van Wüllen, *J. Chem. Phys.*, 1998, **109**, 392–399.

56 F. Weigend and R. Ahlrichs, *Phys. Chem. Chem. Phys.*, 2005, **7**, 3297–3305.

57 D. A. Pantazis, X.-Y. Chen, C. R. Landis and F. Neese, *J. Chem. Theory Comput.*, 2008, **4**, 908–919.

58 F. Neese, F. Wennmohs, A. Hansen and U. Becker, *Chem. Phys.*, 2009, **356**, 98–109.

59 R. Izsák and F. Neese, *J. Chem. Phys.*, 2011, **135**, 144105.

60 F. Weigend, *Phys. Chem. Chem. Phys.*, 2006, **8**, 1057–1065.

61 J. Kästner, J. M. Carr, T. W. Keal, W. Thiel, A. Wander and P. Sherwood, *J. Phys. Chem. A*, 2009, **113**, 11856–11865.

62 V. Barone and M. Cossi, *J. Phys. Chem. A*, 1998, **102**, 1995–2001.

63 B. Benediktsson and R. Bjornsson, *J. Chem. Theory Comput.*, 2022, **18**, 1437–1457.

64 A. T. Thorhallsson, B. Benediktsson and R. Bjornsson, *Chem. Sci.*, 2019, **10**, 11110–11124.

65 B. Benediktsson, A. T. Thorhallsson and R. Bjornsson, *Chem. Commun.*, 2018, **54**, 7310–7313.

66 D. Lukoyanov, V. Pelmenschikov, N. Maeser, M. Laryukhin, T. C. Yang, L. Noddleman, D. R. Dean, D. A. Case, L. C. Seefeldt and B. M. Hoffman, *Inorg. Chem.*, 2007, **46**, 11437–11449.

67 J. Kim and D. C. Rees, *Science*, 1992, **257**, 1677–1682.

68 Y. Xiao, M. Koutmos, D. A. Case, D. Coucounanis, H. Wang and S. P. Cramer, *Dalton Trans.*, 2006, 2192–2201.

69 J. Christiansen, P. J. Goodwin, W. N. Lanzilotta, L. C. Seefeldt and D. R. Dean, *Biochemistry*, 1998, **37**, 12611–12623.

70 E. Jimenez-Vicente, Z. Y. Yang, W. K. Ray, C. Echavarri-Erasun, V. L. Cash, L. M. Rubio, L. C. Seefeldt and D. R. Dean, *J. Biol. Chem.*, 2018, **293**, 9812–9823.

71 C. Van Stappen, E. Jiménez-Vicente, A. Pérez-González, Z.-Y. Yang, L. C. Seefeldt, S. DeBeer, D. R. Dean and L. Decamps, *Chem. Sci.*, 2022, **13**, 3489–3500.

72 T. Spatzal, K. A. Perez, O. Einsle, J. B. Howard and D. C. Rees, *Science*, 2014, **345**, 1620–1623.

73 W. Kang, C. C. Lee, A. J. Jasniewski, M. W. Ribbe and Y. Hu, *Science*, 2020, **368**, 1381–1385.

74 T. Spatzal, K. A. Perez, J. B. Howard and D. C. Rees, *eLife*, 2015, **4**, e11620.

75 Z. Li, J. Li, N. S. Dattani, C. J. Umrigar and G. K.-L. Chan, *J. Chem. Phys.*, 2019, **150**, 024302.

76 Z. Li, S. Guo, Q. Sun and G. K.-L. Chan, *Nat. Chem.*, 2019, **11**, 1026–1033.

77 S. Sharma, K. Sivalingam, F. Neese and G. K.-L. Chan, *Nat. Chem.*, 2014, **6**, 927–933.

